RGNZ/MGPB

Analysis of the Impact of the Hunga-Tonga Eruption on January 15, 2022, on Ionospheric Disturbances Using GNSS TEC

Rudarsko-geološko-naftni zbornik
(The Mining-Geology-Petroleum Engineering Bulletin)
DOI: 10.17794/rgn.2026.5.7

Original scientific paper

Paisa Paisa[1], Buldan Muslim[2], Satria Bijaksana[1]*, Rizal Suryana[3], Khalil Ibrahim[1], Ulvienin Harlianti[1]

[1] *Faculty of Mining and Petroleum Engineering, Institut Teknologi Bandung, Jalan Ganesa 10, Bandung 40132, Indonesia.*
[2] *Research Center for Climate and Atmosphere, National Research and Innovation Agency (BRIN), Bandung, Indonesia.*
[3] *Aeronautics and Space Research Center, National Research and Innovation Agency (BRIN), Bogor, Indonesia.*

Abstract

This study investigates global ionospheric disturbances triggered by the 2022 Hunga Tonga–Hunga Ha'apai (HTHH) eruption using high-resolution GNSS-TEC data from 25 observation stations. Spectral analysis identifies a complex multi-period structure comprising four distinct wave components. Period I, interpreted as a Lamb wave and the primary energy carrier, propagated with a horizontal phase velocity of 330.9 ± 4.3 m/s. Period II, representing the transition from supersonic shock waves to global-scale gravity waves, exhibited a velocity of 270.6 ± 19.7 m/s. Period III, associated with atmospheric gravity waves, propagated at 253.6 ± 19.0 m/s, while period IV, linked to vertical acoustic resonance, showed a velocity of 358.2 ± 14.0 m/s. A notable observation is the presence of extreme amplitude anomalies at the HKSL (Hong Kong) station, reaching up to 25.0 TECU. This enhancement is attributed to constructive interactions between the propagating waves and local ionospheric electrodynamics, particularly the Pre-Reversal Enhancement (PRE) phenomenon. In contrast, the near-source region is characterised by ionospheric depletion (ionospheric hole) caused by strong shock-acoustic impulses. These findings highlight that the intensity of volcanic-induced ionospheric disturbances is strongly controlled by local electrodynamic conditions. Moreover, the observed velocity differences between ionospheric disturbances and oceanic tsunamis demonstrate the potential of GNSS-TEC as a complementary approach for future volcanic tsunami hazard monitoring.

Keywords:
HTHH eruption; TEC; GNSS; Lamb waves; internal gravity waves

1. Introduction

The HTHH volcanic eruption, which occurred on January 15, 2022 in the South Pacific Ocean, was recorded as one of the most energetic volcanic events in modern history (see **Figure 1**). With a Volcanic Explosivity Index (VEI) of 5–6, the eruption attracted global attention due to its exceptional explosive intensity and the widespread damage it caused in Tonga (**Matoza et al., 2022; Lynett et al., 2022**). The highly pressurised, gas-rich magmatic system (H_2O, CO_2, and SO_2) triggered a climactic phase that injected a significant amount of water vapour into the stratosphere (**Henley et al., 2024; Carn et al., 2022**). Uniquely, unlike tsunamis typically driven by seafloor tectonic deformation, the trans-oceanic tsunami generated by HTHH spread at a much faster rate than predicted by conventional models. Recent studies have confirmed that this tsunami was driven by atmospheric pressure waves (Lamb atmospheric waves) that propagated rapidly over the sea surface through an air-sea coupling mechanism, or meteotsunami (**Omira et al., 2022; Kubota et al., 2022**).

Prior to the catastrophic event of 2022, HTHH had shown intermittent eruptive activity, including Surtseyan events in 2009 and 2014-2015 that altered the island morphology (**Carn et al., 2022**). However, the 2022 eruption exhibited fundamentally different characteristics due to the dominance of atmospheric disturbances. The generated shock waves not only triggered acoustic waves and Lamb waves on the surface, but also propagated vertically, triggering global ionospheric disturbances detected as significant variations in Total Electron Content (TEC) (**Chernogor, 2023**). As a layer of the atmosphere rich in free electrons, the ionosphere is highly sensitive to disturbances from below (lower atmosphere forcing), particularly from impulsive explosions that experience exponential amplification as they propagate to the thinner upper layers. The electrodynamic impact of these disturbances was even confirmed through geomagnetic observations, where previ-

* Corresponding author: Satria Bijaksana
e-mail address: satria@itb.ac.id
Received: 19 December 2025. Accepted: 11 May 2026.
Available online: 26 October 2026

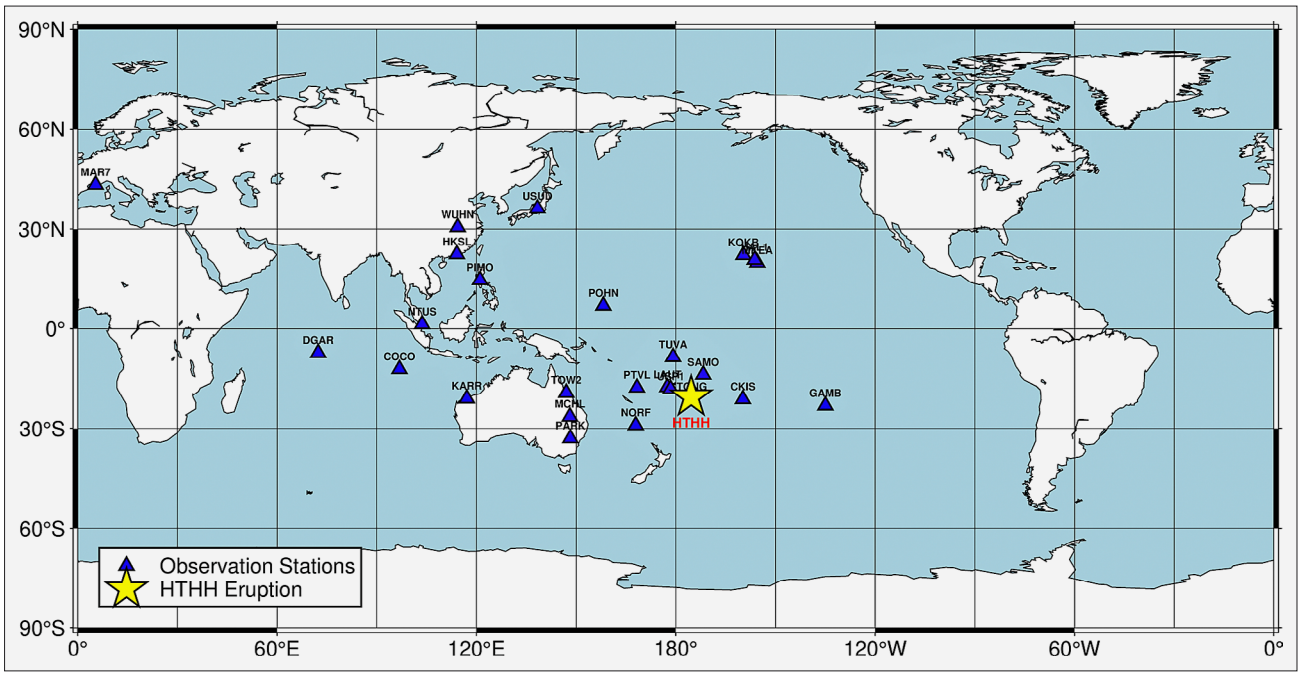


Figure 1: Global map of the observation stations (blue triangles) and the HTHH eruption source (yellow star) in the Pacific Ocean.

ous studies detected vertical acoustic resonance and intense ionospheric dynamo currents immediately following the eruption (**Iyemori et al., 2022; Shimizu et al., 2025**).

Previous research has provided a comprehensive understanding of the global propagation of these disturbances. Several studies have confirmed that Lamb waves functioned as the main energy carriers, non-dispersively triggering TEC disturbances across various regions, from New Zealand and Australia to Japan and Southeast Asia (**Heki, 2022; Muafiry et al., 2022; Muafiry et al., 2023; Flores & Macalalad, 2024**). In Japan, despite moderate TEC fluctuations, traces of these waves were observed to propagate around the Earth multiple times (**Fu et al., 2025; Zhang et al., 2022; Saito, 2022**). Even in regions with low geomagnetic latitudes, such as Peru, **Pacheco et al. (2024)** recorded significant TEC variability. In addition to horizontal propagation analysis, **Cahyadi et al. (2024)** made significant contributions by using 3D tomography to map the vertical structure of ionospheric disturbances, which correlated with tsunami activity.

Although the primary atmospheric waves generated by the HTHH eruption have been widely identified in global-scale studies, a significant gap in understanding remains. Most previous works tend to emphasise a single dominant wave mode, particularly Lamb waves, while the spectral characteristics of internal gravity waves (IGWs) and high-frequency acoustic modes are often not examined separately or in sufficient detail (**Zhang et al., 2022; Heki, 2022**). Moreover, numerous studies concentrate exclusively on the eruption day, neglecting a systematic comparison with a quiet reference day (e.g. January 14, 2022), which is crucial for differentiating genuine ionospheric disturbances from background variability.

This study addresses these gaps by analysing atmospheric wave behaviour using a multi-period filtering approach. The ionospheric response is separated into four spectral bands (Periods I–IV), allowing us to compare a range of disturbance types, from nondispersive Lamb waves to vertical acoustic resonance. We also examine the HKSL station (Hong Kong) in more detail, where an unusually large amplitude anomaly of 25.0 TECU was observed. We interpret this feature as a possible result of coupling between eruption-driven wave perturbations and the pre-reversal enhancement (PRE), an interaction that has received limited attention in previous studies. By comparing TEC variations on the quiet day and the eruption day, we further distinguish the different responses observed in the near-field and far-field regions and assess the role of local electrodynamic conditions in shaping the ionospheric disturbance.

2. Data and Methods

2.1. Data Acquisition and Preprocessing

This study employs Global Navigation Satellite System (GNSS) observation data obtained from 25 International GNSS Service (IGS) stations with global geographic distribution (see **Table 1**). The stations were carefully selected to support a comparative analysis between near-field ionospheric responses and far-field equatorial effects, including those observed at the HKSL station (see **Figure 1**). The dataset is provided in Receiver Independent Exchange Format (RINEX) with a

Table 1: Stations of the Global Navigation Satellite System that are related to the HTHH Volcano.

No.	Station Code	Latitude (°)	Longitude (°)	Radial Distance (km)	Direction (azimuth) from HTHH (°)
1	LAUT	-21.14	-175.20	398	160.0 (Southeast)
2	USP1	-17.80	-178.65	431	310.1 (Northwest)
3	PTVL	-20.65	-170.21	844	91.6 (East)
4	TONG	-19.96	-174.01	1049	38.7 (Northeast)
5	NORF	-29.04	167.94	1254	263.8 (West)
6	TUVA	-21.41	-179.91	1399	254.9 (Southwest)
7	SAMO	-14.28	-170.70	1610	43.7 (Northeast)
8	CKIS	-21.21	-159.78	2755	93.1 (East)
9	MCHL	-17.74	178.81	3091	299.7 (Northwest)
10	TOW2	-19.64	179.37	3148	301.9 (Northwest)
11	PARK	-32.89	148.33	3312	255.4 (Southwest)
12	POHN	6.96	158.20	3599	305.8 (Northwest)
13	KOKB	-31.78	115.89	5486	272.7 (West)
14	GAMB	-23.13	-134.97	5518	94.3 (East)
15	MKEA	19.82	-155.46	5525	34.1 (Northeast)
16	HAL1	-42.80	147.25	5556	250.3 (Southwest)
17	KARR	-26.87	113.84	6470	275.5 (West)
18	PIMO	4.88	150.84	7182	307.7 (Northwest)
19	USUD	18.23	117.84	7514	307.2 (Northwest)
20	HKSL	22.31	114.21	8322	308.7 (Northwest)
21	COCO	12.05	96.84	8768	297.8 (Northwest)
22	WUHN	30.54	114.36	8833	309.4 (Northwest)
23	NTUS	25.01	121.54	8833	309.4 (Northwest)
24	DGAR	-7.28	72.37	11529	288.7 (Northwest)
25	MAR7	-63.51	-59.50	19728	126.8 (Southeast)

temporal resolution of 30 seconds, which is crucial for capturing rapid ionospheric disturbances such as Travelling Ionospheric Disturbances (TIDs) induced by volcanic eruptions.

Station selection was based on data quality criteria, including signal integrity and continuity, assessed through a low frequency of cycle slips and a stable signal-to-noise ratio (SNR). Furthermore, a satellite elevation mask greater than 10° was applied to reduce potential multipath interference. For efficient data storage, the observations were initially downloaded in compressed Compact RINEX (CRX) format and later converted into standard RINEX (RNX) format for processing using MATLAB 2016a (https://www.mathworks.com). During preprocessing, essential parameters were extracted, including observation time, Pseudo-Random Noise (PRN), L1 and L2 carrier phase measurements, and satellite geometry (elevation and azimuth). These parameters were then organised into a structured tabular format to facilitate numerical analysis and Total Electron Content (TEC) computation.

2.2. TEC Processing and Bias Elimination

The core of this methodology involves calculating the Slant Total Electron Content (STEC) to quantify the total number of electrons along the signal path between the satellite and the receiver. In this study, STEC was deliberately used instead of vertical TEC (VTEC) to preserve high sensitivity for detecting small-amplitude ionospheric disturbances. While VTEC provides a normalised measurement by applying a geometric mapping function, this conversion can introduce artificial noise and smoothing effects, especially at low satellite elevation angles. For rapid geophysical events such as the HTHH eruption, using raw STEC allows for capturing line-of-sight phase fluctuations with higher fidelity. The raw Slant Total Electron Content ($STEC_{raw}$) is calculated by applying a linear combination of the L1 and L2 carrier phase measurements, as presented in **Equation 1**. This approach follows the well-established methodologies outlined by **Mannucci et al., 1998**, **Sardón et al., 1994, and Tang et al., 2014**.

$$\mathrm{STEC}_{raw} = \frac{f_1^2 f_2^2}{40.3(f_1^2 - f_2^2)}[(\lambda_1\Phi_1 - \lambda_2\Phi_2)\text{-}$$

$$\text{-}(\lambda_1 N_1 - \lambda_2 N_2)\text{-}b_f - B_f] \quad (1)$$

where:

f_1, f_2 are the GNSS carrier frequencies (L1 = 1575.42 MHz, L2 = 1227.60 MHz),

λ_1, λ_2 are the wavelengths of the carrier signals ($\lambda = c/f$),

Φ_1, Φ_2 are the carrier phase measurements (cycles),

N_1, N_2 represent the integer phase ambiguities,

b_f, B_f denote the satellite and receiver instrumental biases, respectively.

A major challenge in using phase data is the presence of the variables N, b_f, and B_f whose absolute values are not recorded in the RINEX files. However, since these variables are constant (time-invariant) during one continuous satellite observation arc, they are recorded as offsets or fixed biases in the data. Therefore, the processing strategy does not require the calculation of these bias values individually. Instead, a 7th-order polynomial fitting method is applied to the raw data. This order selection aims to model and remove the slow ionospheric background variation trend ($STEC_{pol}$) (**Equation 2**), such as the daily solar effect without removing the high-frequency disturbance signals generated by the eruption (**Ozeki & Heki, 2010**).

$$STEC_{pol} = A_0 + A_1 \sum_{n=1}^{N} X^n \quad (2)$$

Where X represents the time of observation, and N is the order of the polynomial used to filter out longer variations than those caused by seismic or meteorological effects in this study, we used N=7.

After obtaining the $STEC_{raw}$ (**Equation 1**) and $STEC_{pol}$ (**Equation 2**), the next step is to compute δTEC (**Equation 3**), which represents the ionospheric disturbance caused by rapid geophysical events, such as volcanic eruptions. δTEC is calculated by subtracting $STEC_{pol}$ from $STEC_{raw}$ **(Ozeki & Heki, 2010; Lay et al., 2013)**:

$$\delta TEC = STEC_{raw} - STEC_{pol} \quad (3)$$

In this subtraction process, the constant offset components from ambiguities (N) and instrument biases (b_f,B_f) are automatically cancelled out or eliminated along with the daily variation trend, leaving only short-term fluctuations purely caused by external disturbances such as eruptions (**Lay et al., 2013**).

The Rate of Total Electron Content (ROT) is derived as the temporal variation of Slant Total Electron Content (STEC), following the approach proposed by **Pi et al. (1997)**. ROT is defined as **Equation 4**:

$$ROT = \frac{STEC_i - STEC_{i-1}}{t_i - t_{i-1}} \quad (4)$$

where:

ROT: Rate of Total Electron Content (TECU/min),

$STEC_i$: Slant Total Electron Content at time t_i (TECU),

$STEC_{i-1}$: Slant Total Electron Content at previous time t_{i-1} (TECU),

$t_i - t_{i-1}$: time interval between consecutive observations (minutes).

To quantify ionospheric irregularities, the Rate of TEC Index (ROTI) is calculated as the standard deviation of ROT within a specified time window. ROTI is expressed as **Equation 5**:

$$ROTI = \sqrt{\langle ROT^2 \rangle - \langle ROT \rangle^2} \quad (5)$$

where:

ROTI: Rate of TEC Index (TECU/min),

$\langle ROT \rangle$: mean value of ROT within the selected time window,

$\langle ROT^2 \rangle$: mean value of squared ROT within the selected time window.

The ROTI parameter is widely used as an indicator of ionospheric irregularities and plasma turbulence, particularly in equatorial and low-latitude regions. Higher ROTI values correspond to stronger electron density fluctuations and enhanced ionospheric disturbances. This method has been validated in previous studies (**Oladipo & Schüler, 2013; Ikani et al., 2023**) and has been widely applied in GNSS-based ionospheric monitoring (**Pi et al., 1997**).

2.3. Multi-Period Spectral Filtering

After applying polynomial filtering to obtain δTEC (**Equation 3**), the data were further processed using multi-period band-pass filtering. This step is crucial for separating δTEC into specific wave components, as the HTHH eruption produced a broad spectrum of atmospheric waves with overlapping frequencies. In this study, filtering was conducted using a zero-phase digital Butterworth filter, implemented via the *filtfilt* function to avoid phase shifts. This procedure was applied directly to the δTEC time-series data using the frequency bands specified in **Table 2**, rather than employing a Fourier-based masking technique. This approach preserves the temporal integrity of wave onsets (T_{obs}) for accurate velocity calculations.

The classification of the four distinct propagation periods is based on the spectral characteristics of ionospheric disturbances observed in recent HTHH studies (**Themens et al., 2022**; **Wright et al., 2022**), which define specific ranges for Lamb waves (P>30 min), gravity waves, and acoustic resonance (~4 min). These period bands are defined to isolate specific atmospheric wave modes. Period I (60–180 minutes) corresponds to primary Lamb waves, which function as the main carriers of energy. Period II (30–60 minutes) and Period III (10–30 minutes) represent the transition toward dispersive internal gravity waves (IGWs). Meanwhile, Period IV (≤ 10 minutes) captures high-frequency acoustic waves as well as vertical resonance processes. By applying these predefined bands, the multi-period filtering approach effectively separates overlapping wave signatures generated by the broad energy spectrum of the eruption, thereby allowing a clearer interpretation of the distinct wave dynamics. Wave arrival times (T_{obs}) were determined

Table 2: Classification of multi-period bandpass filters

Wave Period	Period Range (T)	Description	Key Reference
Period I	60 – 180 min	Longest period	**Themens et al. (2022)**
Period II	30 – 60 min	Intermediate	**Wright et al. (2022)**
Period III	10 – 30 min	Intermediate	**Zhang et al. (2022)**
Period IV	≤ 10 min	Shortest period	**Iyemori et al. (2022)**

manually through visual inspection of the first wave peaks that significantly deviated from the quiet-day noise level (January 14, 2022). This visual criterion, supported by recent diagnostic frameworks for the Tonga event (**Zhang et al., 2022**; **Pacheco et al., 2024**), allows for accurate identification of wave onset amid complex, multi-modal signatures. Subsequently, the peak amplitudes of the isolated waves were measured for energy attenuation and propagation analyses.

2.4. Kinematic Analysis and Spatial Visualisation

After isolating δTEC using the multi-period band-pass filters, the propagation characteristics were analysed using the time–distance method. This method correlates the radial distance (D) of each station from the eruption source with the wave travel time (ΔT). The horizontal propagation velocity (v) for each wave period was inferred from the gradient (slope) of the linear regression (*best-fit line*) on the time–distance plot. This technique is a standard method for estimating the phase velocity of travelling ionospheric disturbances and has been widely validated in global studies of Lamb wave propagation following major eruptions (**Zhang et al., 2022**). The regression analysis was performed to obtain the best observational velocity estimates for Lamb waves, IGWs, and acoustic waves.

In the final stage of the analysis, the software tools were divided according to their specific roles. Python was used to conduct numerical calculations of phase velocity and to generate time–distance hodograms for Periods I, II, III, and IV. Python was used to process numerical Δt and D data and to perform linear regression for determining the best-fit phase velocity. The resulting hodogram plots allow visual inspection of the linearity between distance and travel time.

For spatial visualisation, the Generic Mapping Tools (GMT) software was used (**Wessel & Smith, 1991**). GMT was employed to create contour maps of velocity and maximum amplitude across all station locations.

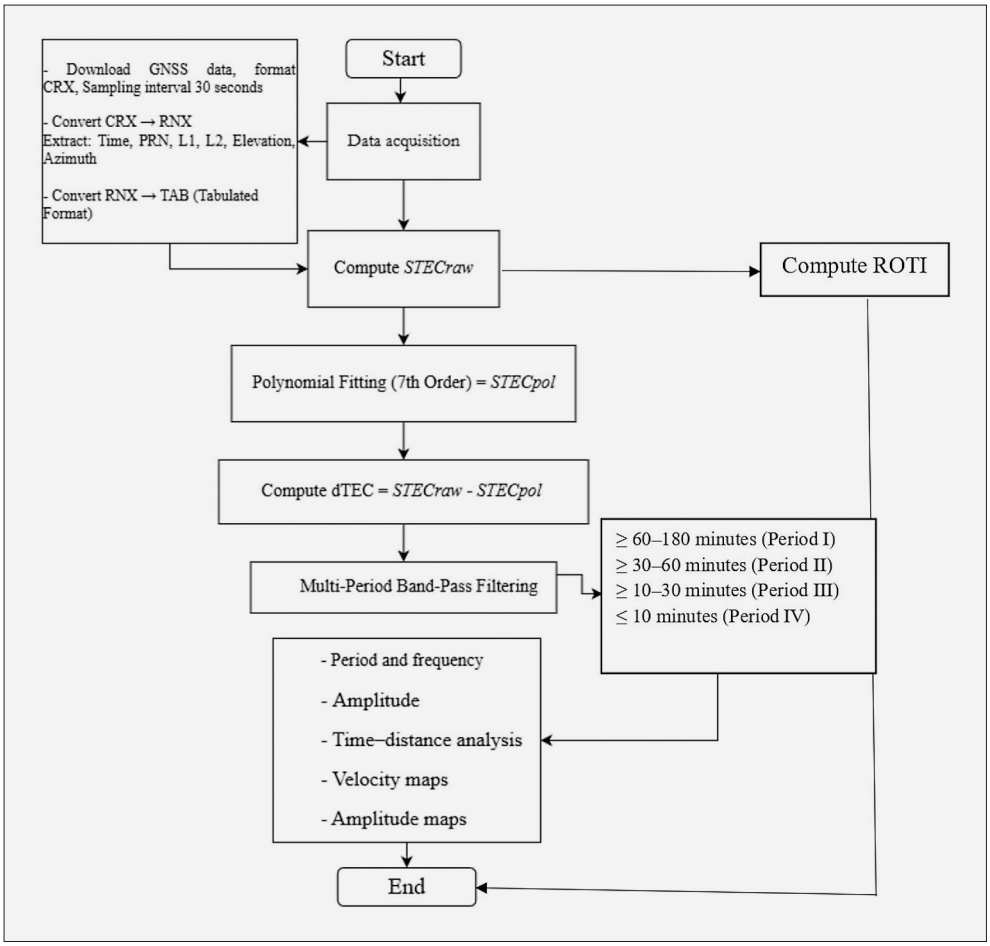


Figure 2: Data processing flowchart

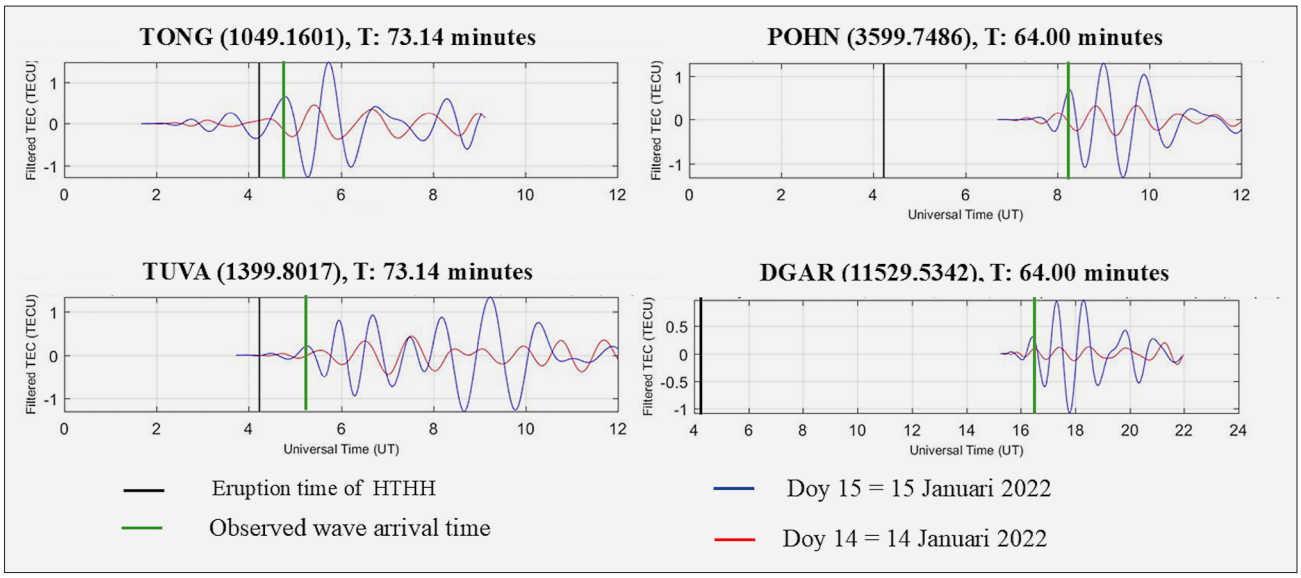


Figure 3: Polynomial-filtered TEC variations for Period I on the eruption day (January 15, 2022; blue) and the quiet day (January 14, 2022; red) at four representative stations: (a) TONG (73.14 min), (b) TUVA (73.14 min), (c) POHN (64.00 min), and (d) DGAR (64.00 min). The green vertical line marks the observed wave arrival time, and the black vertical line marks the eruption time of HTHH.

These maps aim to illustrate the spatial distribution of wave energy in the Pacific region and to identify potential propagation anomalies, such as directional asymmetry or variations in signal intensity with respect to distance and azimuth. The complete methodological workflow, from data acquisition, polynomial bias removal, and multi-period filtering to kinematic analysis and spatial visualisation, is summarised in the research flowchart (see **Figure 2**) to ensure reproducibility.

3. Results

In this study, the ionospheric response was analysed by comparing observations from the eruption day (January 15, 2022) and a quiet reference day (January 14, 2022), with the eruption time fixed at 04:15 UT. The δTEC variations across GNSS stations are presented in **Figures 3 – 6**, where the eruption-day data are shown in blue and the quiet-day data in red. The onset of ionospheric disturbances is indicated by a green vertical line, while the eruption reference time (04:15 UT) is marked by a black vertical line in each panel (**Figures 3**, **4**, **5** and **6**). Stations located closer to the eruption source recorded earlier with more distinct responses.

For Period I (see **Figure 3**), the selected stations include TONG (1049 km; 73.14 min), TUVA (1399 km; 73.14 min), POHN (3599 km; 64.00 min), and DGAR (11529 km; 64.00 min). The eruption-day signal appears earlier at the nearer stations, around 4.7–5.6 UT at TONG and TUVA, and later at the more distant stations, around 8.1 UT at POHN and about 16.0 UT at DGAR. Compared with the quiet day, the eruption-day response is more clearly developed after the marked arrival time and shows broader, more coherent oscillations. At the TONG station (1049 km), the fastest disturbance (Period IV) was detected at 05:12 UT, followed by Period II at 05:21 UT. These signals exhibit sharper amplitudes compared to background fluctuations on the quiet day. A similar pattern is observed at the USP1 station (431 km), where Period II arrived at 05:30 UT. At greater distances, such as the SAMO station (1610 km), disturbances were detected slightly later, with the simultaneous arrival of multiple components at 05:35 UT (see **Figure 4**). Overall, the systematic delay in arrival times with increasing distance indicates outward propagation of ionospheric disturbances from the eruption source.

A similar distance-dependent delay is also observed for Period II (see **Figure 4**), represented by TONG (51.20 min), SAMO (56.89 min), USUD (46.54 min), and DGAR (56.89 min). In this case, the filtered waveforms show greater differences in amplitude and waveform shape between stations. The response is visible near 5.0–5.3 UT at TONG and SAMO, while it appears later at USUD, around 7.8 UT, and at DGAR, around 15.0 UT. Period III (see **Figure 5**) is characterized by shorter wave packets, with representative periods of 26.22 min at TONG, 20.48 min at SAMO, 10.66 min at USUD, and 28.44 min at DGAR. The eruption-day signal becomes increasingly localized in time, particularly at USUD and DGAR, where the filtered oscillations appear as more compact wave trains after the marked arrival times.

The shortest-period response is shown in Period IV (see **Figure 6**), with periods of 8.25 min at TONG, 8.00 min at SAMO, 9.84 min at USUD, and 9.84 min at DGAR. These waveforms remain clearly identifiable across the selected stations, but they are more compact in time and generally smoother than those of Periods II and III. As in the other bands, the onset shifts systemati-

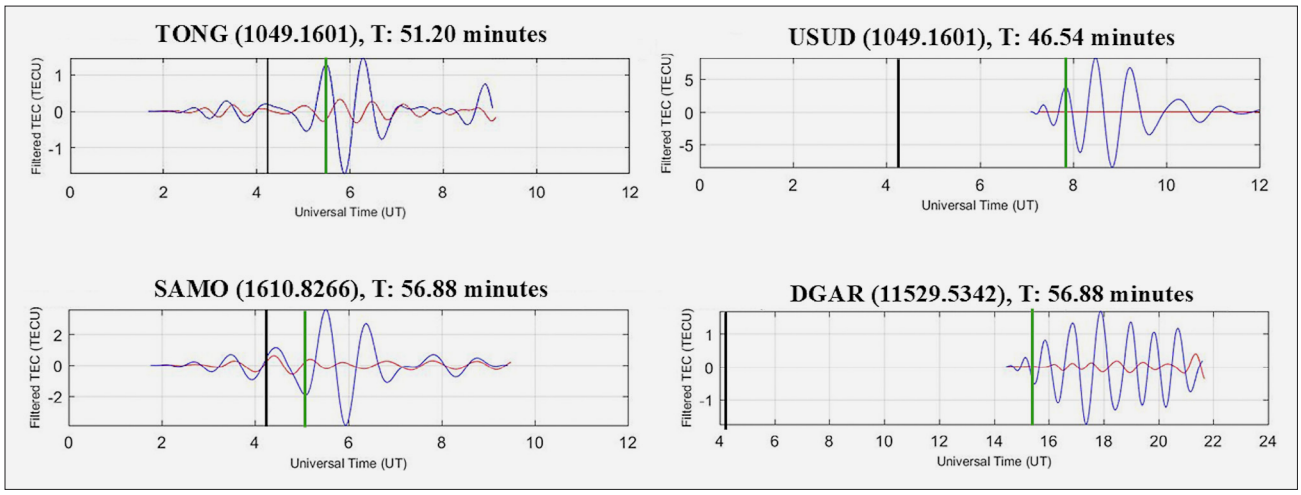


Figure 4: Band-pass filtered TEC variations for Period II at four representative stations: (a) TONG (51.20 min), (b) SAMO (56.89 min), (c) USUD (46.54 min), and (d) DGAR (56.89 min). The colour scheme and vertical reference lines are the same as in **Figure 3**.

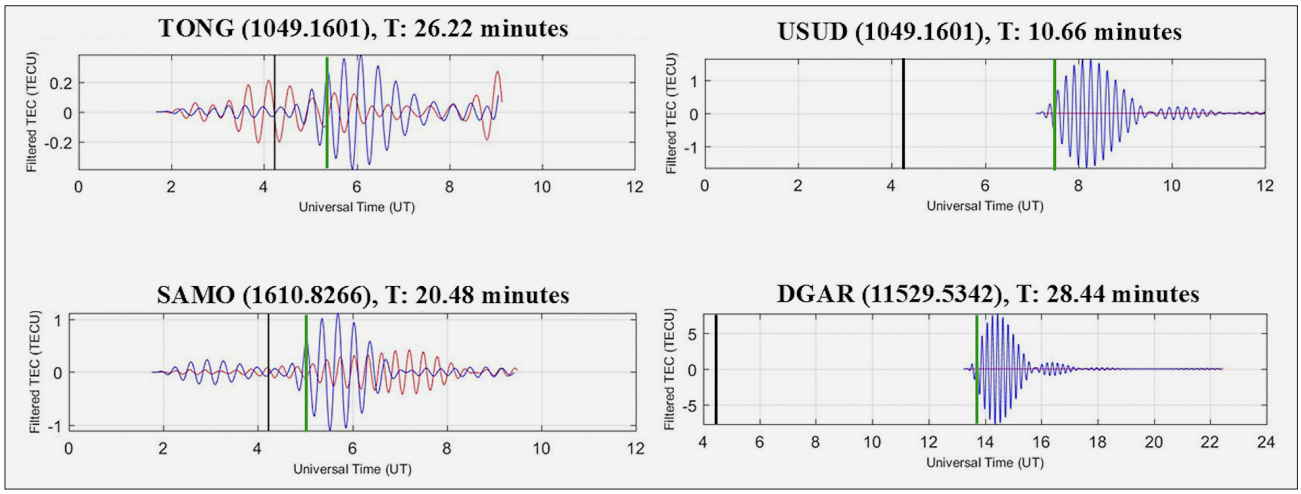


Figure 5: Band-pass filtered TEC variations for Period III at four representative stations: (a) TONG (26.22 min), (b) SAMO (20.48 min), (c) USUD (10.66 min), and (d) DGAR (28.44 min). The colour scheme and vertical reference lines are the same as in **Figure 3**.

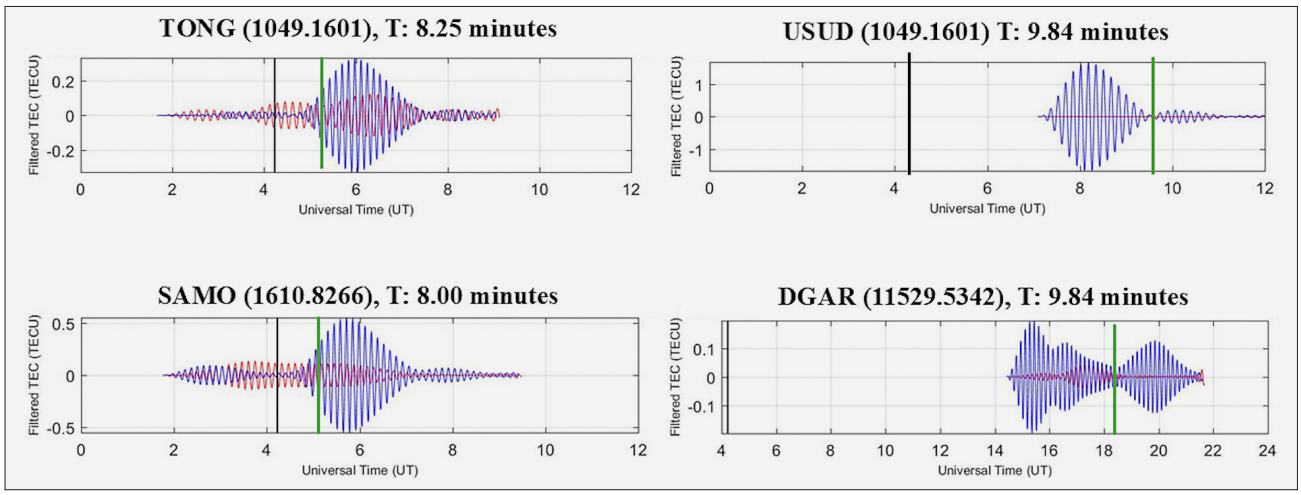


Figure 6: Band-pass filtered TEC variations for Period IV at four representative stations: (a) TONG (8.25 min), (b) SAMO (8.00 min), (c) USUD (9.84 min), and (d) DGAR (9.84 min). The colour scheme and vertical reference lines are the same as in **Figure 3**.

Table 3: Summary of representative wave periods observed across the GNSS network.

Station	Distance (km)	PRN	Period I (min)	Period II (min)	Period III (min)	Period IV (min)
LAUT	398	23	73.14	42.67	26.95	**4.61**
USP1	431	23	73.14	42.67	20.48	**4.53**
PTVL	844	23	64	39.38	22.26	8.53
TONG	1049	23	73.14	51.2	22.26	8.26
NORF	1254	23	64	51.2	26.95	7.88
TUVA	1399	32	73.14	56.89	28.44	8
SAMO	1610	23	64	56.89	20.48	8
CKIS	2755	23	64	56.89	28.44	9.85
MCHL	3091	32	64	42.67	26.95	9.31
TOW2	3148	32	64	32	13.47	8
PARK	3312	31	64	39.38	14.63	8.98
POHN	3599	16	64	51.2	28.44	9.48
KOKB	5486	26	64	42.67	28.44	9.14
GAMB	5518	32	64	56.89	18.96	9.14
MKEA	5525	26	64	51.2	26.95	9.48
HAL1	5556	26	64	51.2	26.95	8.83
KARR	6470	22	73.14	32	25.6	9.14
PIMO	7182	14	64	56.89	24.38	3.3
USUD	7514	8	73.14	46.55	10.67	9.85
HKSL	8322	17	73.14	51.2	25.6	9.48
NTUS	8833	2	102.4	30.12	11.13	9.94
COCO	8833	15	64	42.67	25.6	9.31
WUHN	8768	20	73.14	51.2	18.96	9.85
DGAR	11529	15	64	56.89	28.44	9.85
MAR7	19728	24	32	28.44	28.44	8.68

cally from the nearer stations to the more distant ones, from about 5.4–5.6 UT at TONG and SAMO to around 7.8 UT at USUD and about 14.5 UT at DGAR. Overall, **Figures 3** – **6** show that the ionospheric response varies systematically with both propagation distance and spectral period, with longer periods producing broader oscillations and shorter periods producing more localized wave packets. **Table 3** summarizes the representative wave periods observed across the GNSS network, highlighting systematic differences in the dominant periods recorded at each station for Periods I–IV.

Table 4 summarises the wave propagation velocities for each period across observation stations located at different distances from the eruption source. In general, the velocities vary between stations, reflecting the non-uniform propagation conditions. Period I exhibits relatively stable velocities compared to the other periods, whereas Periods II and III show greater variability, indicating a stronger influence of local conditions and atmospheric dynamics. In contrast, Period IV displays a more consistent pattern with relatively higher velocities. Overall, the variation in velocities across periods and stations suggests that ionospheric disturbance propagation is controlled not only by the eruption source but also by atmospheric conditions along the propagation path.

The hodogram analysis in **Figure 7** reveals variations in wave propagation velocities across different periods. Period I (see **Figure 7a**) shows a velocity of 330.9 ± 4.3 m/s with a strong linear relationship (R^2=0.988), indicating stable and coherent propagation. In contrast, Period II and period III (see **Figures 7b, c**) exhibit lower velocities of 270.6 ± 19.7 m/s and 253.6 ± 19.0 m/s, respectively, along with weaker correlations (R^2=0.651 and R^2=0.635), suggesting greater variability and stronger influence of local atmospheric conditions. Period IV (**Figure 7d**) shows an increased velocity of 358.2 ± 14.0 m/s with a relatively strong correlation (R^2=0.891), indicating a more organised propagation pattern. Overall, the differences in velocity and correlation strength among the periods reflect the multi-mode nature of ionospheric wave propagation, controlled by both source dynamics and atmospheric conditions. These results support the interpretation of Period I as a Lamb wave, Period II as a transition from shock-acoustic to gravity wave regimes, Period III as internal gravity waves, and Period IV as vertical acoustic resonance, as illustrated in **Figure 7.**

The wave arrival time (T_{obs}) was determined through visual inspection of the first wave peak that significantly deviated from the noise level on a quiet day (January 14,

Table 4: Wave speeds for four periods at various stations

No.	Station	Distance (km)	*v* Period I (m/s)	*v* Period II (m/s)	*v* Period III (m/s)	*v* Period IV (m/s)
1	LAUT	398	144.20	265.33	60.30	150.11
2	USP1	431	143.67	287.33	68.41	155.20
3	PTVL	844	200.95	468.89	122.32	250.60
4	TONG	1049	233.11	**1,165.56**	205.69	194.26
5	NORF	1254	220.00	220.00	199.05	205.50
6	TUVA	1399	259.07	310.89	274.31	265.40
7	SAMO	1610	315.69	894.44	536.67	357.80
8	CKIS	2755	316.67	540.20	417.42	417.42
9	MCHL	3091	318.00	228.96	210.27	310.25
10	TOW2	3148	314.17	**1,165.93**	218.61	355.20
11	PARK	3312	298.38	245.33	193.68	310.15
12	POHN	3599	307.61	255.25	239.93	325.60
13	KOKB	5486	315.29	651.33	499.71	360.10
14	GAMB	5518	322.69	347.04	259.06	340.50
15	MKEA	5525	323.10	472.22	472.22	400.90
16	HAL1	5556	324.91	377.96	474.87	561.30
17	KARR	6470	326.77	552.99	798.77	553.00
18	PIMO	7182	342.00	342.39	298.21	390.10
19	USUD	7514	343.11	610.89	610.89	610.10
20	HKSL	8322	342.47	308.22	280.20	350.25
21	NTUS	8833	350.52	288.66	285.86	355.40
22	WUHN	8833	346.39	205.90	192.44	345.50
23	COCO	8768	347.94	191.02	191.02	370.20
24	DGAR	11529	320.25	284.67	284.67	312.45

Note: Identical velocity values at specific stations result from the 30-second GNSS sampling resolution and the arrival of wave components as a coherent packet (**Themens et al., 2022**). These values represent the best observable approximation within technical constraints.

2022). It is important to acknowledge that this manual identification involves an observable approximation due to the 30-second sampling interval of the GNSS data. This technical limitation introduces a small margin of uncertainty, as the actual wave arrival may occur between sampling intervals.

Therefore, identical velocity values recorded at some stations (e.g. NORF, MKEA, and DGAR) for different wave periods should be understood as the closest observable estimates within the technical constraints of the dataset. When the onsets of multiple wave components occur within the same 30-second sampling window, both are timestamped identically, resulting in identical velocities for a fixed distance. Additionally, this pattern reflects the physical phenomenon in which these components arrive as coherent wave packets before significant atmospheric dispersion occurs, consistent with recent observations of HTHH ionospheric waves (**Themens et al., 2022**).

Figure 8 illustrates the relationship between propagation velocity and distance from the eruption source across all GNSS observation stations. Overall, the distribution reveals a clear variability in wave propagation characteristics as a function of distance, indicating the presence of multiple wave modes generated by the HTHH eruption. At intermediate to far-field distances, most velocity values cluster within the range of ~200–350 m/s, which is consistent with typical atmospheric gravity waves and Lamb wave propagation. These modes dominate the general trend, showing relatively stable velocities over increasing distance, suggesting large-scale energy propagation through the atmosphere. In detail, Period I shows an increase from relatively lower values in the near-field region to a more stable range of approximately 320–350 m/s at greater distances. Period II exhibits the largest variability, including two prominent high-velocity peaks at TONG and TOW2, indicating strong local effects near the source. Period III also shows considerable variability, with several elevated values at intermediate and far-field distances. Period IV displays a more gradual increase with distance and a narrower velocity range in the far field.

In contrast, several stations exhibit significantly higher velocities exceeding 1000 m/s, particularly within specific distance ranges. These high-velocity values do not follow a uniform spatial trend and appear as scattered anomalies. Such observations may reflect apparent

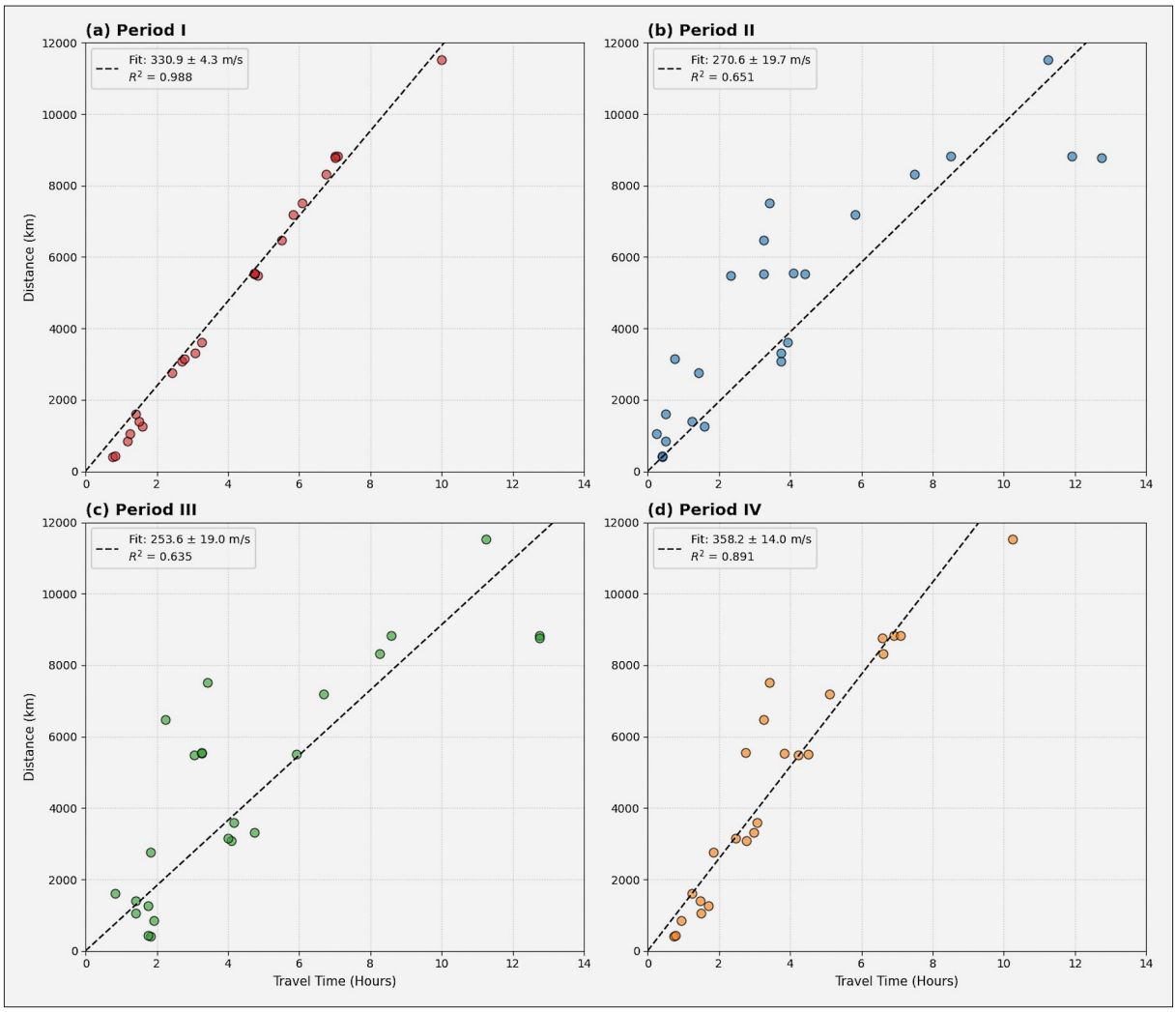


Figure 7: Hodograph analysis of horizontal phase velocity for four ionospheric wave periods following the HTHH eruption. Symbols represent observations from 25 GNSS stations, and dashed lines show the linear regression fits used to estimate mean propagation velocity. (a) Period I: 330.9 ± 4.3 m/s (R^2 = 0.988); (b) Period II: 270.6 ± 19.7 m/s (R^2 = 0.651); (c) Period III: 253.6 ± 19.0 m/s (R^2 = 0.635); and (d) Period IV: 358.2 ± 14.0 m/s (R^2 = 0.891).

horizontal phase velocities influenced by wavefront geometry, propagation direction, and the interaction of multiple wave modes. Although these values are commonly associated with acoustic or shock-related disturbances generated by explosive events, their interpretation requires caution, as GNSS-TEC observations do not directly measure true physical propagation speeds. Overall, the figure demonstrates that ionospheric disturbances following the HTHH eruption cannot be described by a single propagation mechanism. Instead, the observed velocity distribution supports the coexistence of gravity waves, Lamb waves, and higher-frequency disturbances, with spatial variability controlled by both source dynamics and atmospheric propagation effects.

The spatial distribution of horizontal phase velocities (see **Figure 9**) reveals distinct propagation characteristics across different periods. Period I exhibits a relatively uniform global pattern, indicating stable large-scale propagation. In contrast, Period II (see **Figure 9b**) shows strong spatial heterogeneity with localised high-velocity anomalies, reflecting the transition from shock-acoustic waves to gravity waves. Period III (see **Figure 9c**) is characterised by moderate velocities and broader spatial dispersion, consistent with atmospheric gravity wave propagation. Meanwhile, Period IV displays more localised variations with relatively higher velocities in specific regions, suggesting the influence of acoustic resonance mechanisms (see **Figure 9d**). Overall, the observed patterns indicate that ionospheric wave propagation is strongly modulated by both source dynamics and background atmospheric conditions.

The amplitude distribution (see **Figure 10**) further demonstrates significant spatial asymmetry in the ionospheric response. Period I shows, in **Figure 10a**, a pronounced energy enhancement in the northern hemisphere, indicating non-uniform energy distribution. A similar pattern persists in Period II (see **Figure 10b**), where disturbance intensity is not strictly controlled by distance from the source but is influenced by regional conditions. For Period III (see **Figure 10c**), the distur-

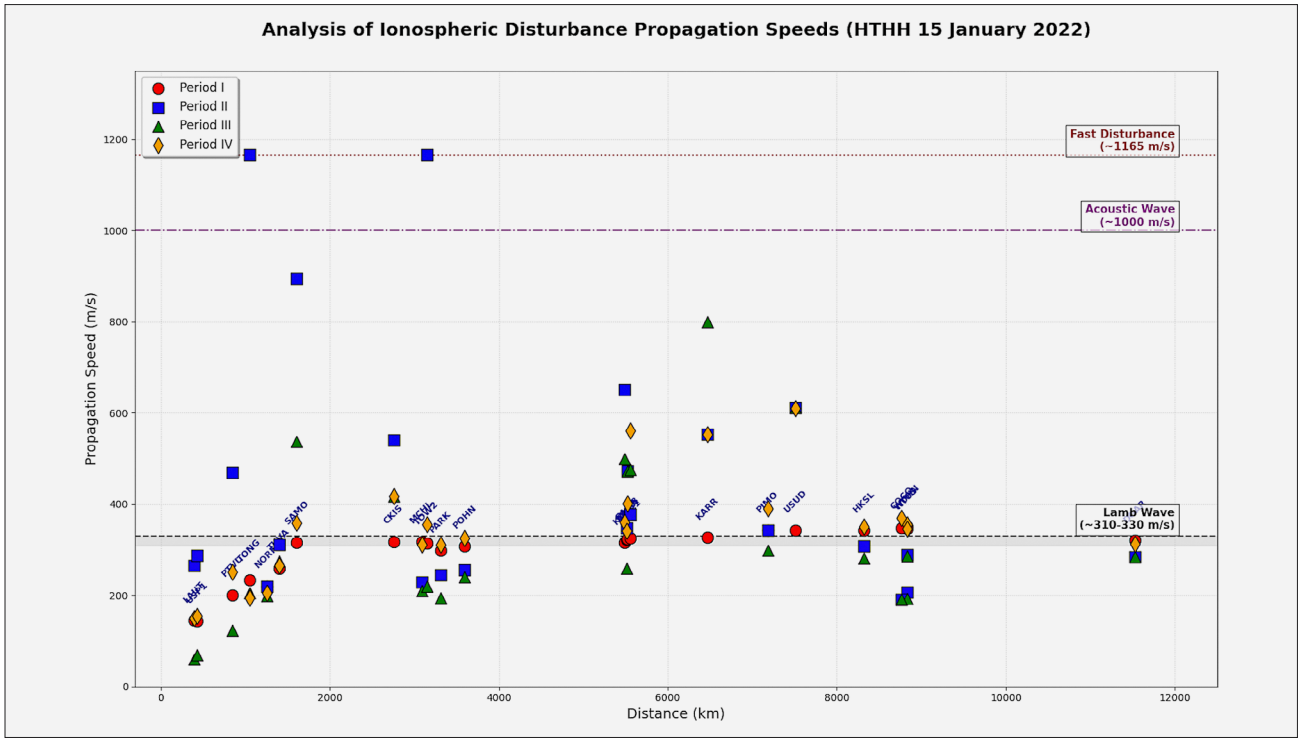


Figure 8: Propagation velocity plotted against distance from the HTHH source for all observation stations. Symbols represent the four disturbance periods, and the horizontal dashed lines mark reference velocity ranges near 330 m/s and ~1000 m/s. The distribution shows substantial variability across stations and periods, with most observations clustering in the ~200–400 m/s range and a smaller number of higher-velocity peaks at selected distances.

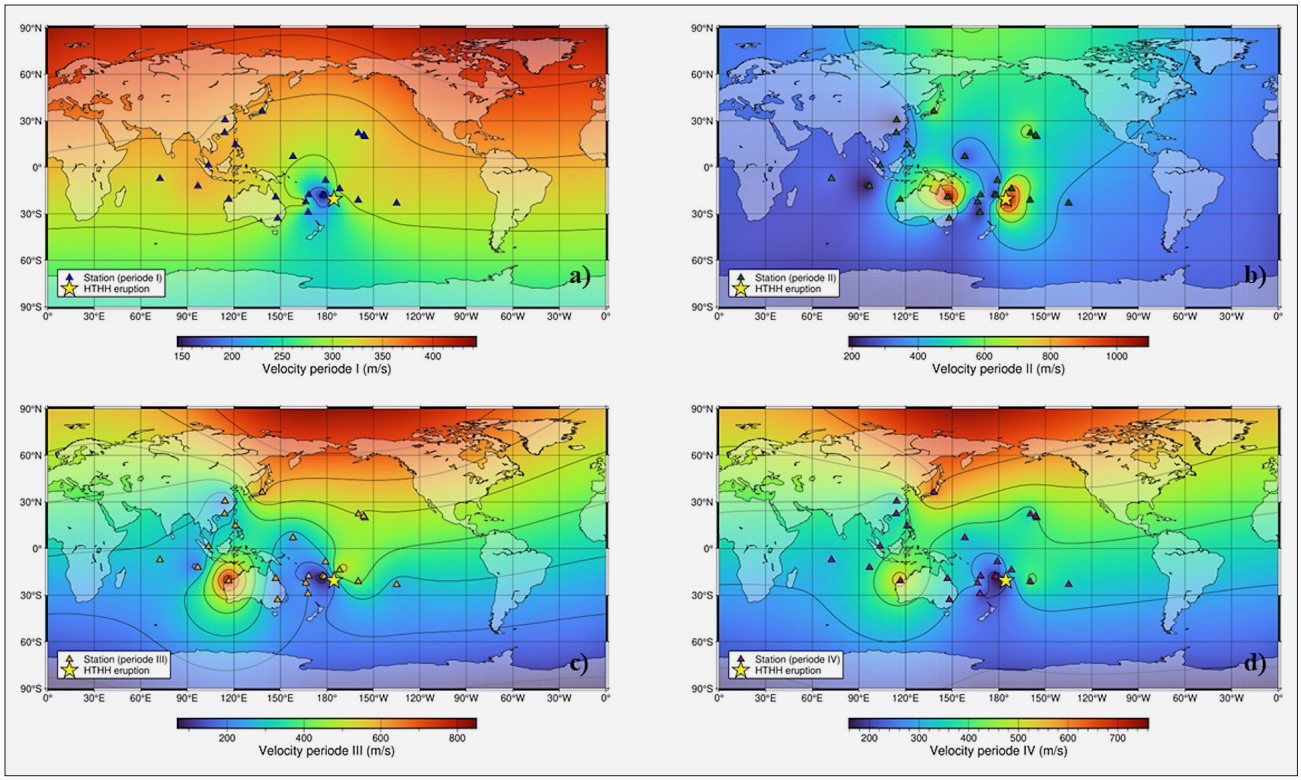


Figure 9: Global spatial distribution of horizontal phase velocities for the four ionospheric disturbance periods following the 2022 HTHH eruption. Colour shading represents velocity magnitude (m/s), and contour lines indicate spatial variations in propagation speed. Triangles mark the 25 GNSS observation stations, and the star denotes the eruption source. Panels (a)–(d) show Periods I–IV, respectively. Period I displays a relatively smooth large-scale pattern, whereas Periods II–IV show progressively stronger regional variability and localized velocity anomalies.

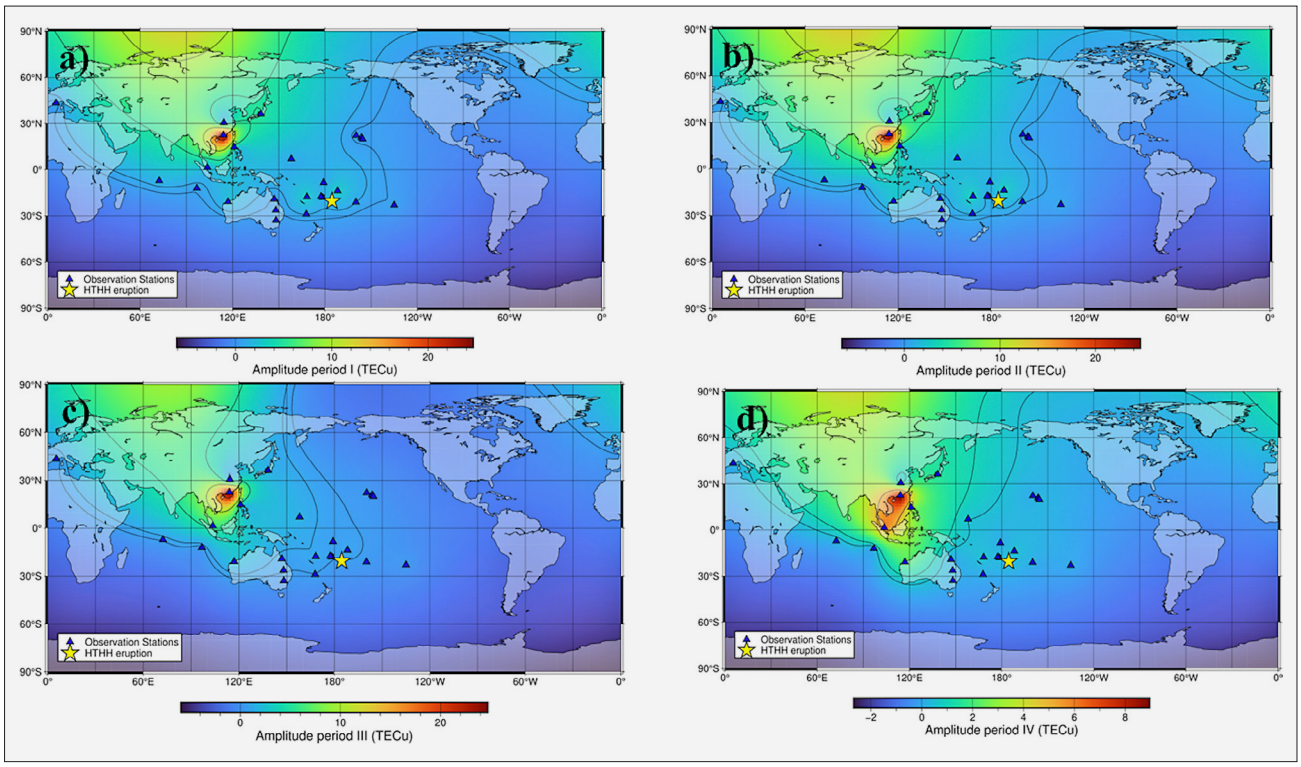


Figure 10: Contour map of the maximum wave amplitude distribution for (a) Period I (δTEC), highlighting extreme amplitude anomalies (>20 TECU) centred in East Asia. (b) Spatial distribution of ionospheric disturbance amplitude for Period II, showing similar energy spread with the largest signal amplification in the northern hemisphere (Asia sector). (c) Wave amplitude distribution for Period III, where disturbance intensity becomes more localised, with high amplitudes in Hong Kong but fading in the Central Pacific region, and (d) Visualisation of wave amplitude for Period IV, where low disturbance energy (<5 TECU) is observed globally, with significant impact only near the eruption centre. The yellow star marks the HTHH eruption, and blue triangles represent GNSS observation stations.

bance becomes more spatially localised, suggesting energy dissipation and reduced large-scale coherence. In contrast, Period IV (see **Figure 10d**) exhibits generally weak amplitudes, indicating limited energy propagation except in regions close to the eruption source. Wave propagation shows generally higher velocities at stations closer to the eruption source, with Period II and Period IV exhibiting broader variability and higher speeds compared to Period I and Period III (see **Figures 10a–10d**).

The quantified strength of ionospheric disturbances at each station is summarised in **Table 5**, which presents the maximum TEC amplitudes. The results indicate a non-linear energy distribution, where disturbance magnitude does not decrease monotonically with distance from the source, suggesting a considerable influence of regional ionospheric and atmospheric conditions.

4. Discussion

Through linear regression analysis (*best-fit slope*) of the travel-time diagrams (see **Figure 7**), the estimated global horizontal phase velocity for the main disturbance in Period I is 330.9 ± 4.3 m/s (see **Figure 7a**). This velocity provides crucial thermodynamic evidence. Physically, the speed of acoustic waves is proportional to the square root of the medium's temperature. The observed value of 330.9 ± 4.3 m/s, although slightly lower than the standard speed of sound at sea level, is highly consistent with the expected velocity of Lamb waves propagating through the lower thermosphere. This is in agreement with the principle proposed by **Heki & Ping (2005)**, which states that ionospheric disturbance propagation reflects the local sound speed at F-region altitudes. Therefore, Period I can be interpreted as a dominant Lamb wave, propagating as a non-dispersive solitary pulse that efficiently guides energy along the Earth's surface without significant attenuation (**Kubota et al., 2022**).

The velocity observed in Period I is also relevant to tsunami generation mechanisms. This ionospheric wave speed falls within the range capable of resonating with deep-ocean gravity waves (~200–220 m/s) (see **Figure 7a**). This further supports the interpretation that the global tsunami triggered by the HTHH eruption was a meteotsunami driven by atmosphere–ocean coupling. The atmospheric pressure perturbation associated with the Lamb wave acts as a "piston", efficiently transferring energy into the ocean and accelerating tsunami propagation beyond predictions based solely on seafloor deformation (**Omira et al., 2022**).

Further analysis of Period II (see **Figure 7b**) reveals more complex dynamics. Based on global *best-fit* regression, Period II exhibits an average velocity of 270.6

Table 5: Wave amplitude for four periods at various stations.

Station	Distance (km)	PRN	Amp. Period I (TECU)	Amp. Period II (TECU)	Amp. Period III (TECU)	Amp. Period IV (TECU)
LAUT	398	23	1.5	1.5	0.6	0.3
USP1	431	23	1.1	0.6	0.6	0.3
PTVL	844	23	3	3	1	0.5
TONG	1049	23	1.5	1.5	0.3	0.4
NORF	1254	23	1	1	0.5	0.06
TUVA	1399	32	1	1	0.5	0.06
SAMO	1610	23	3	3	1	0.5
CKIS	2755	23	1	0.6	0.2	0.1
MCHL	3091	32	0.5	0.6	0.6	0.2
TOW2	3148	32	0.3	0.6	0.6	0.02
PARK	3312	31	0.2	0.2	0.2	0.06
POHN	3599	16	1	1.5	1.5	0.5
KOKB	5486	26	0.3	0.4	0.2	0.03
GAMB	5518	32	0.6	0.6	0.3	0.06
MKEA	5525	26	0.4	0.2	0.06	0.3
HAL1	5556	26	0.3	0.4	0.2	0.04
KARR	6470	22	2.1	2.2	2.5	2.3
PIMO	7182	14	3	3	3	3
USUD	7514	8	5.1	5.5	1.5	1.5
HKSL	8322	17	**25**	**25**	**25**	**9**
NTUS	8833	2	1.5	**4**	**6**	**6**
COCO	8833	15	0.6	0.4	0.2	0.05
WUHN	8768	20	0.6	1	0.3	0.3
DGAR	11529	15	1.5	1.5	0.6	0.2
MAR7	19728	24	0.2	0.2	0.2	0.04

± 19.7 m/s (see **Figure 7b**), generally characteristic of internal gravity waves. However, station-level analysis shows significant variability, particularly at near-field stations such as TONG, where impulsive supersonic velocities reach 1165.56 m/s (see **Table 4**). The discrepancy between the relatively low global velocity (~270.6 m/s) and the very high local values suggests that Period II represents a transitional or hybrid phase. The observation of exceptionally high velocities exceeding 1000 m/s during Period II at several near-field stations (e.g. TONG and TOW2) requires careful physical interpretation. These values are significantly higher than the typical speed of sound in the lower atmosphere (~290–340 m/s). In this study, such values are interpreted as apparent horizontal phase velocities rather than true propagation speeds. This phenomenon arises because the ionospheric pierce point (IPP) represents the projection of the wavefront movement onto a horizontal plane. Immediately after the Hunga Tonga–Hunga Ha'apai (HTHH) eruption, the disturbance propagates as a supersonic shock wave through the thermosphere. In regions close to the source, the orientation of the wavefront, combined with a strong vertical propagation component, leads to an overestimation of horizontal velocities. As the propagation distance increases, these shock waves gradually dissipate and transition into dispersive atmospheric gravity waves and Lamb waves. Consequently, the observed velocities tend to stabilise within the expected physical range of the thermosphere (**Salby, 1996; Wallace & Hobbs, 2006**).

Meanwhile, Period III (see **Figure 7c**), with a *best-fit* velocity of 253.6 ± 19.0 m/s (see **Figure 7c**), exhibits more stable characteristics as a sequence of secondary gravity waves. These waves are interpreted as products of energy dissipation in the mesosphere, consistent with the model proposed by **Vadas et al. (2023)**.

Findings related to vertical acoustic resonance in Period IV (see **Figure 9** and **Table 2**) reveal a direct relationship between the electron density oscillation period observed at stations USP1 and LAUT (~4.53 minutes) and the magnetic disturbance period of ~4.61 minutes (see **Table 3**), as reported by **Iyemori et al. (2022)**. This indicates an active ionospheric dynamo mechanism, in which vertically resonant waves force ionospheric plasma to oscillate across geomagnetic field lines. This motion induces electric currents through the Lorentz force, consistent with ionospheric electrodynamics principles described by **Kelley (2009)**. This mechanism is further

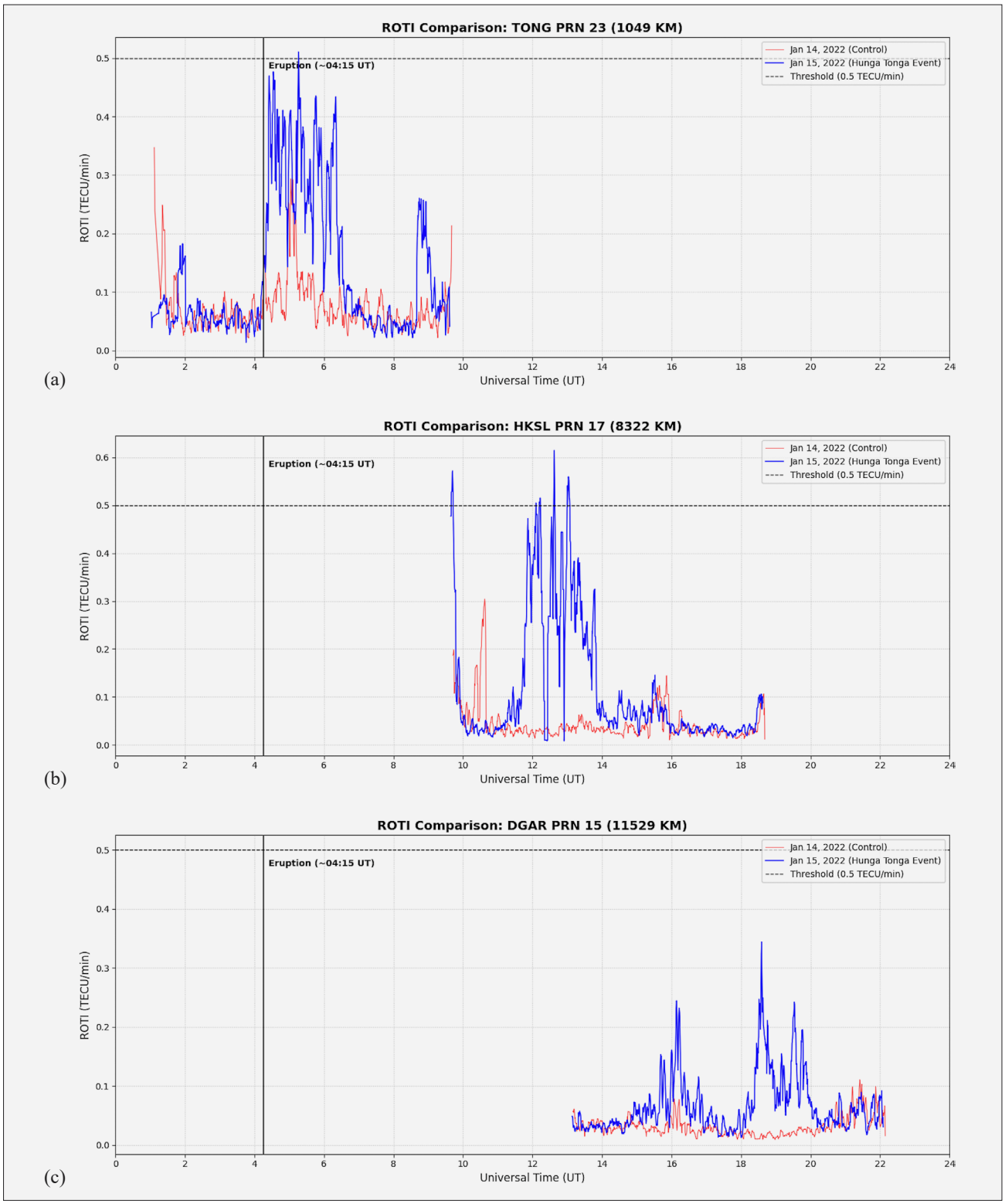


Figure 11: Comparison of the ROTI between the quiet day (January 14, 2022) and the eruption day (January 15, 2022) at three GNSS stations located at different distances from the Hunga Tonga–Hunga Ha'apai (HTHH) source. The vertical solid line marks the eruption time (~04:15 UT), and the horizontal dashed line indicates the disturbance threshold (0.5 TECU/min). (a) TONG (~1049 km), (b) HKSL (~8322 km), and (c) DGAR (~11529 km) show clear differences in the timing and amplitude of the ROTI response, with earlier and stronger variations at the nearer station and progressively later responses at greater distances.

confirmed by **Shimizu et al. (2025)** using magnetometer data from the 'Atele (TBU), Tongatapu station, validating the mechanical origin of electromagnetic disturbances in the near-field region.

Table 6: Wave period speed and its physical implications post-HTHH eruption

Wave Period	Speed (v) / global best fit	Shape characteristics	Physical mechanism interpretation
Period I	330.9 ± 4.3 m/s	Dominant pulse (single peak)	Lamb waves are the main stable waves propagating globally.
Period II	270.6 ± 19.7 m/s (Note: Local variability up to 500–1000 m/s)	Fast impulse and oscillation	Hybrid phase: the hybrid phase behaves globally as a gravity wave but contains acoustic/shock wave components at specific stations.
Period III	253.6 ± 19.0 m/s	Wave series	Secondary gravity waves are stable and sustained oscillations.
Period IV	358.2 ± 14.0 m/s	Short Period (~4.00 minutes)	In acoustic resonance, vertical atmospheric oscillation (up-down) is trapped.

The most significant energy distribution anomaly is observed at the HKSL station (Hong Kong), where amplitudes reach 25.0 TECU (see **Table 5**), far exceeding values near the source (e.g. TONG: 1.5 TECU). This extreme enhancement is hypothesised to result from constructive interaction between the propagating Lamb wave and the Pre-reversal Enhancement (PRE) mechanism in the equatorial region. Although direct ionosonde or in situ measurements are unavailable, ROTI analysis (**Pi et al., 1997**; **Oladipo & Schüler, 2013**) provides strong supporting evidence, showing a sharp increase exceeding 0.5 TECU/min, occurring synchronously with wave arrival during the post-sunset Period (~19:00 LT).

Based on high-resolution GNSS-TEC data, this study reconstructs the ionospheric response to the HTHH eruption. The disturbance position was projected at a reference altitude of 350 km, representing the thermospheric layer where maximum electron density typically occurs. The comparison of ROTI values between the control day and the eruption day (see **Figure 11**) reveals clear temporal and spatial differences across stations. At the near-field station **Figure 11a** (TONG), ROTI values increase rapidly shortly after the eruption time (~04:15 UT), exceeding the disturbance threshold. At the intermediate-distance station (HKSL) (see **Figure 11b**), enhanced ROTI values are observed several hours after the eruption, with larger fluctuations compared to the control day. Meanwhile, the far-field station (DGAR) shows a delayed response with relatively lower ROTI values. Overall (see **Figure 11c**), the ROTI patterns indicate a time-dependent and distance-dependent ionospheric response to the eruption (see **Figure 11**).

The temporal coincidence between the PRE phase, atmospheric wave arrival, and enhanced ROTI strongly suggests that volcanic disturbances function as a seeding mechanism for the development of large-scale Equatorial Plasma Bubbles (EPBs) and plasma turbulence (**Aa et al., 2022**; **Flores & Macalalad, 2024**). This interpretation is further supported by previous studies demonstrating that equatorial ionospheric irregularities are sensitive to post-sunset electrodynamic conditions and can be significantly amplified under favourable background conditions (**Ikani et al., 2023**). These findings are consistent with global observations reported by **Astafyeva (2019)**, as well as with the "super bubble" characteristics described by **Themens et al. (2022)**.

Figure 9 and **Figure 10** together show that the ionospheric response to the Hunga Tonga–Hunga Ha'apai eruption varied with both spectral period and spatial scale. Period I is characterized by a relatively smooth velocity field near ~330 m/s and a broad amplitude distribution, which is consistent with previous studies describing large-scale Lamb-wave propagation after the HTHH eruption (**Wright et al., 2022**; **Muafiry et al., 2022**; **Muafiry et al., 2023**). In contrast, Periods II and III show stronger spatial variability in both velocity and amplitude, with localized regions of enhanced values. This pattern is consistent with reports that the HTHH eruption generated a broad spectrum of acoustic-gravity disturbances rather than a single uniform propagation mode (**Inchin et al., 2023**; **Figueiredo et al., 2023**). Period IV displays more localized velocity and amplitude patterns, suggesting reduced spatial coherence at shorter periods. Enhanced amplitudes in the East Asia sector may also indicate that local ionospheric conditions contributed to the observed response, although this interpretation should be treated cautiously without independent electrodynamic measurements (**Shinbori et al., 2023; Pacheco et al., 2024**).

In addition, the global characteristics of Period I indicate the potential for wave superposition at the antipodal point. Based on the estimated phase velocity of 330.9 ± 4.3 m/s (see **Figure 7a**), waves propagating in multiple directions are expected to reconverge in North Africa approximately 16.7 hours after the eruption. Although the farthest station (MAR7) did not record extreme amplitude enhancement on the first day, global studies by **Zhang et al. (2022)** confirm that these waves can circumnavigate the Earth up to three times. This suggests that antipodal superposition likely occurred, although its ionospheric impact may be highly localised or outside the observation window. Furthermore, the observed ionospheric wave speed for Period I (330.9 ± 4.3 m/s; see **Figure 7a**) highlights the conceptual potential of GNSS-TEC observations to complement tsunami early warning systems. This velocity exceeds the typical speed of deep-ocean tsunami waves (~200–220 m/s), thereby theoretically providing valuable lead time, as the ionospheric

signature can be detected at distant stations prior to the arrival of the oceanic wave. However, translating this conceptual advantage into practical implementation requires addressing several operational challenges, including real-time data streaming latency, the development of robust automated detection algorithms, and the integration of GNSS-TEC observations with existing seismic and sea-level monitoring networks. Thus, while these findings validate the physical basis for early detection, further research focused on real-time operational frameworks is essential for fully realising their practical utility in hazard mitigation. As a synthesis of the overall kinematic and dynamic analysis, the physical characteristics of the four wave periods are comprehensively summarised in **Table 6**. This table classifies each period based on global phase velocity, signal morphology, and underlying physical mechanisms, providing a complete picture of the ionospheric response to the HTHH eruption.

5. Conclusions

This study shows that the HTHH eruption caused highly complex ionospheric disturbances with multi-period characteristics. Period I (Lamb wave) was identified as the main energy carrier with a speed of 330.9 ± 4.3 m/s, which is consistent with the meteo-tsunami mechanism. Period IV in the near-field region showed characteristics of vertical acoustic resonance with a period of about 4.53 – 4.61 minutes, validating the detected geomagnetic disturbances. Meanwhile, the spatial amplitude distribution of the disturbances was strongly influenced by local electrodynamic phenomena, such as the formation of plasma bubbles in Hong Kong and ionospheric holes in Tonga, reflecting the ionospheric response to the event. Future studies could explore more advanced filtering techniques, such as the Savitzky-Golay filter (**Zhang et al., 2009; 2022**), to compare their performance with polynomial fitting in capturing high-frequency ionospheric disturbances.

Acknowledgement

This investigation received comprehensive financial backing from the Indonesian Endowment Fund for Education (LPDP). The authors also recognise the assistance provided by the facilities and infrastructure rendered by Institut Teknologi Bandung (ITB). The analysis of the data for this study was significantly enhanced through the use of the following software: Generic Mapping Tools (GMT) for the visualisation and mapping of geophysical data; MATLAB for the processing and modelling of data; and Python for scientific computation and spectral analysis.

6. References

Aa, E., Zhang, S.-R., Erickson, P. J., Vierinen, J., Coster, A. J., Goncharenko, L. P., Spicher, A., & Rideout, W. (2022). Significant ionospheric hole and equatorial plasma bubbles after the 2022 Tonga volcano eruption. *Space Weather*, *20*(7), e2022SW003101. https://doi.org/10.1029/2022SW003101

Astafyeva, E. (2019). Ionospheric detection of natural hazards. *Reviews of Geophysics*, *57*(4), 1265–1288. https://doi.org/10.1029/2019RG000668

Cahyadi, M. N., Muslim, B., Muafiry, I. N., Gusman, A. R., Handoko, E. Y., Anjasmara, I. M., Yasyukevich, Y., & Yasyukevich, A. (2024). 3D Traveling Ionospheric Disturbances During the 2022 Hunga Tonga–Hunga Ha'apai Eruption Using GNSS TEC. *Journal of Geophysical Research: Space Physics*, *129*(4), e2023JA031806. https://doi.org/10.1029/2023JA031806

Carn, S. A., Krotkov, N. A., Fisher, B. L., & Li, C. (2022). Out of the blue: Volcanic SO_2 emissions during the 2021-2022 eruptions of Hunga Tonga-Hunga Ha'apai (Tonga). *Frontiers in Earth Science*, *10*, 976962. https://doi.org/10.3389/feart.2022.976962

Chernogor, L. F. (2023). Ionospheric total electron content variations caused by the Tonga volcano explosion on January 15, 2022. *Kosmichna Nauka i Tekhnologiya*, *29*(3), 67–87. https://doi.org/10.15407/knit2023.03.067

Figueiredo, C. A., Vadas, S. L., Becker, E., Wrasse, C. M., Takahashi, H., Nyassor, P. K., & Barros, D. (2023). Secondary gravity waves from the Tonga volcano eruption: Observation and modeling over New Zealand and Australia. *Journal of Geophysical Research: Space Physics*, *128*(10). https://doi.org/10.1029/2023ja031476

Flores, G. M. J., & Macalalad, E. P. (2024). Electron density variations in the ionosphere associated with the Tonga volcanic eruption in 2022 over Southeast Asia using Global Navigation Satellite Systems. *2024 IEEE 4th International Conference on Automation, Control, and Energy Systems (ACES)*,1–6.https://doi.org/10.1109/acee62618.2024.00017

Fu, Z., Shen, X., Liu, Q., & Wang, N. (2025). Ionospheric disturbances from the 2022 Hunga-Tonga volcanic eruption: Impacts on TEC spatial gradients and GNSS positioning accuracy across the Japan region. *Remote Sensing*, *17*(17), 3108. https://doi.org/10.3390/rs17173108

Heki, K. (2022). Ionospheric signatures of repeated passages of atmospheric waves by the 2022 Jan. 15 Hunga Tonga-Hunga Ha'apai eruption detected by QZSS-TEC observations in Japan. *Earth, Planets and Space*, *74*(1), 1–12. https://doi.org/10.1186/s40623-022-01674-7

Heki, K., & Ping, J. (2005). Directivity and apparent velocity of the coseismic ionospheric disturbances observed with a dense GPS array. *Earth and Planetary Science Letters*, *236*(3-4), 845–855. https://doi.org/10.1016/j.epsl.2005.06.010

Henley, R. W., de Ronde, C. E. J., Arculus, R. J., Hughes, G., Pham, T.-S., Casas, A. S., Titov, V., & Walker, S. L. (2024). The 15 January 2022 Hunga (Tonga) eruption: A gas-driven climactic explosion. *Journal of Volcanology and Geothermal Research*, *451*, 108077. https://doi.org/10.1016/j.jvolgeores.2024.108077

Ikani, O., Okeke, F. N., Okpala, K. C., Okoh, D., & Rabiu, B. (2023). Diurnal and seasonal variations of the occurrence of ionospheric irregularities over Nigeria from GNSS data.

Frontiers in Astronomy and Space Sciences, *10*. https://doi.org/10.3389/fspas.2023.1125950

Inchin, P. A., Bhatt, A., Cummer, S. A., Eckermann, S. D., Harding, B. J., Kuhl, D. D., Ma, J., Makela, J. J., Sabatini, R., & Snively, J. B. (2023). Multi-layer evolution of acoustic-gravity waves and ionospheric disturbances over the United States after the 2022 Hunga Tonga volcano eruption. *AGU Advances*, *4*(6). https://doi.org/10.1029/2023av000870

Iyemori, T., Nishioka, M., Otsuka, Y., & Shinbori, A. (2022). A confirmation of vertical acoustic resonance and field-aligned current generation just after the 2022 Hunga Tonga-Hunga Ha'apai volcanic eruption. *Earth, Planets and Space*, *74*, Article 103. https://doi.org/10.1186/s40623-022-01653-y

Kubota, T., Saito, T., & Nishida, K. (2022). Global fast-traveling tsunamis driven by atmospheric lamb waves on the 2022 Tonga eruption. Science, 377(6601), 91-94. https://doi.org/10.1126/science.abo4364

Kelley, M. C. (2009). *The Earth's ionosphere: Plasma physics and electrodynamics* (2nd ed.). Academic Press.

Lay, E. H., Shao, X.-M., & Carrano, C. S. (2013). Variation in total electron content above large thunderstorms. *Geophysical Research Letters*, *40*(10), 1945–1949. https://doi.org/10.1002/grl.50499

Lynett, P. J., McCann, M. P., Zhou, Z., Renteria, W., Borrero, J. C., Greer, D., ... & Cinar, G. E. (2022). Diverse tsunamigenesis triggered by the Hunga Tonga-Hunga Ha'apai eruption. *Nature*, *609*(7928), 728–733. https://doi.org/10.1038/s41586-022-05170-6

Mannucci, A. J., Wilson, B. D., Yuan, D. N., Ho, C. M., Lindqwister, U. J., & Runge, T. F. (1998). A global mapping technique for GPS-derived ionospheric total electron content. *Radio Science*, 33(3), 565–582. https://doi.org/10.1029/97RS02707

Matoza, R. S., Fee, D., Assink, J. D., Iezzi, A. M., Green, D. N., Kim, K., ... & Wilson, D. C. (2022). Atmospheric waves and global seismoacoustic observations of the January 2022 Hunga eruption, Tonga. *Science*, *377*(6601), 95–100. https://doi.org/10.1126/science.abo7063

Muafiry, I. N., Meilano, I., Heki, K., Wijaya, D. D., & Nugraha, K. A. (2022). Ionospheric disturbances after the 2022 Hunga Tonga-hunga Ha'apai eruption above Indonesia from GNSS-TEC observations. *Atmosphere*, *13*(10), 1615. https://doi.org/10.3390/atmos13101615

Muafiry, I. N., Wijaya, D. D., Meilano, I., & Heki, K. (2023). Diverse ionospheric disturbances by the 2022 Hunga Tonga-Hunga Ha'apai eruption observed by a dense GNSS array in New Zealand. *Journal of Geophysical Research: Space Physics*, *128*(11), e2023JA031486. https://doi.org/10.1029/2023JA031486

Oladipo, O.A. & Schüler, T. (2013). Equatorial ionospheric irregularities using GPS TEC derived index. *Journal of Atmospheric and Solar-Terrestrial Physics*, 92, 78–82. https://doi.org/10.1016/j.jastp.2012.09.019

Omira, R., Ramalho, R. S., Kim, J., Baptista, M. A., Pelties, C., Cadoux, A., Costa, A., Baptista, P., Dogan, G. G., Yalciner, A. C., & Cetin, M. A. (2022). Global Tonga tsunami explained by a fast-moving atmospheric source. *Nature*, 609(7928), 734–740. https://doi.org/10.1038/s41586-022-04926-x

Ozeki, M., & Heki, K. (2010). Ionospheric holes made by ballistic missiles from North Korea detected with a Japanese dense GPS array. *Journal of Geophysical Research: Space Physics*, *115*(A9), A09314. https://doi.org/10.1029/2010JA015531

Pacheco, E. E., Velasquez, J. P., Flores, R., Condori, L., Fajardo, G., Kuyeng, K., & Manay, E. (2024). The impact of the Hunga Tonga–Hunga Ha'apai volcanic eruption on the Peruvian atmosphere: From the sea surface to the ionosphere. *Earth, Planets and Space*, *76*, Article 79. https://doi.org/10.1186/s40623-024-02022-7

Pi, X., Mannucci, A. J., Lindqwister, U. J., & Ho, C. M. (1997). Monitoring of global ionospheric irregularities using the worldwide GPS network. *Geophysical Research Letters*, 24, 2283–2286. https://doi.org/10.1029/97GL02273

Sardón, E., Rius, A., & Zarraoa, N. (1994). Estimation of the transmitter and receiver differential biases and the ionospheric total electron content from Global Positioning System observations. *Radio Science*, 29(3), 577–586. https://doi.org/10.1029/94RS00449

Shimizu, H., Ishihara, Y., Vaiomounga, R., & Kula, T. (2025). Magnetic field variations in Tongatapu caused by Hunga Tonga-Hunga Ha'apai volcanic activity in January 2022. *Earth, Planets and Space*, *77*, Article 188. https://doi.org/10.1186/s40623-025-02315-5

Saito, S. (2022). Ionospheric disturbances observed over Japan following the eruption of Hunga Tonga-Hunga Ha'apai on 15 January 2022. *Earth, Planets and Space*, *74*(1). https://doi.org/10.1186/s40623-022-01619-0

Salby, M. L. (1996). *Fundamentals of Atmospheric Physics*. Academic Press. ISBN: 9780126151954.

Shinbori, A., Sori, T., Otsuka, Y., Nishioka, M., Perwitasari, S., Tsuda, T., Kumamoto, A., Tsuchiya, F., Matsuda, S., Kasahara, Y., Matsuoka, A., Nakamura, S., Miyoshi, Y., & Shinohara, I. (2023). Generation of equatorial plasma bubble after the 2022 Tonga volcanic eruption. *Scientific Reports*, *13*(1). https://doi.org/10.1038/s41598-023-33603-3

Tang, W., Jin, L., & Xu, K. (2014). Performance analysis of ionosphere monitoring with BeiDou CORS observational data. *The Journal of Navigation*, 67(3), 511–522. https://doi.org/10.1017/S0373463313000854

Themens, D. R., Watson, C., Žagar, N., Vasylkevych, S., Elvidge, S., McCaffrey, A., & Yasyukevich, Y. (2022). Global propagation of ionospheric disturbances associated with the 2022 Tonga volcanic eruption. *Geophysical Research Letters*, *49*(7), e2022GL098158. https://doi.org/10.1029/2022GL098158

Vadas, S. L., Figueiredo, C., Becker, E., Huba, J. D., Themens, D. R., Hindley, N. P., & Sternovsky, Z. (2023). Traveling ionospheric disturbances induced by the secondary gravity waves from the Tonga eruption on 15 January 2022: Modeling with MESORAC-HIAMCM-SAMI3 and comparison with GPS/TEC and ionosonde data. *Journal of Geo-*

physical Research: Space Physics, *128*(6), e2023JA031408. https://doi.org/10.1029/2023JA031408

Wallace, J. M., & Hobbs, P. V. (2006). *Atmospheric Science: An Introductory Survey* (2nd ed.). Academic Press. https://doi.org/10.1016/B978-0-12-733344-1.X5000-3

Wessel, P., & Smith, W. H. F. (1991). Free software for helping condense oceanographic data. *EOS Transactions American Geophysical Union*, 72(41), 441-446. https://doi.org/10.1029/90EO00319

Wright, C. J., Hindley, N. P., Alexander, M., Barlow, M., Hoffmann, L., Mitchell, C. N., & Yue, J. (2022). Surface-to-space atmospheric waves from Hunga Tonga–Hunga Ha'apai eruption. *Nature*, *609*(7928), 741–746. https://doi.org/10.1038/s41586-022-05012-5

Zhang, D. H., Zhang, W., & Xiao, Z. (2009). The influence of geomagnetic storms on the estimation of GPS instrumental biases. *Annales Geophysicae*, 27(4), 1613–1623. https://doi.org/10.5194/angeo-27-1613-2009

Zhang, S.-R., Vierinen, J., Aa, E., Goncharenko, L. P., Erickson, P. J., Rideout, W. C., Coster, A. J., & Spicher, A. (2022). 2022 Tonga volcanic eruption induced global propagation of ionospheric disturbances via Lamb waves. *Frontiers in Astronomy and Space Sciences*, *9*, 871275. https://doi.org/10.3389/fspas.2022.871275

SAŽETAK

Analiza utjecaja erupcije Hunga Tonge od 15. siječnja 2022. na ionosferske poremećaje korištenjem GNSS TEC-a

Ova studija istražuje globalne ionosferske poremećaje potaknute erupcijom Hunga Tonge – Hunga Ha'apaija (HTHH) iz 2022. godine primjenom GNSS-TEC podataka visoke razlučivosti s 25 promatračkih postaja. Spektralna analiza otkriva složenu višeperiodnu strukturu koja se sastoji od četiriju različitih valnih komponenata. Period I, interpretiran kao Lambov val i primarni nositelj energije, širio se horizontalnom faznom brzinom od 330,9 ± 4,3 m/s. Period II, koji predstavlja prijelaz od nadzvučnih udarnih valova do gravitacijskih valova globalnih razmjera, pokazao je brzinu od 270,6 ± 19,7 m/s. Period III, povezan s atmosferskim gravitacijskim valovima, širio se brzinom od 253,6 ± 19,0 m/s, dok je period IV, povezan s vertikalnom akustičnom rezonancijom, imao brzinu od 358,2 ± 14,0 m/s. Važno opažanje jest prisutnost anomalija ekstremne amplitude na postaji HKSL (Hong Kong), koje dosežu do 25,0 TECU. Ovo pojačanje pripisuje se konstruktivnim interakcijama između propagirajućih valova i lokalne ionosferske elektrodinamike, osobito fenomenu *Pre-Reversal Enhancement* (PRE). Nasuprot tome, područje blizu izvora karakterizira ionosfersko iscrpljenje (ionosferska rupa) uzrokovano snažnim udarno-akustičnim impulsima. Ti rezultati ističu da je intenzitet ionosferskih poremećaja izazvanih vulkanima snažno kontroliran lokalnim elektrodinamičkim uvjetima. Nadalje, uočene razlike u brzinama između ionosferskih poremećaja i oceanskih cunamija pokazuju potencijal GNSS-TEC metode kao dopunskoga pristupa za buduće praćenje opasnosti od vulkanskih cunamija.

Ključne riječi:
HTHH erupcija, TEC, GNSS, Lambovi valovi, unutarnji gravitacijski valovi

Author's contribution

Paisa Paisa (BEng, Physicist with expertise in Geographic Information Systems research) was responsible for the integration of data and the final analysis, conducted the data processing, led the analysis of the results, and composed the original drafting. **Buldan Muslim** (Dr, Professor specialising in ionospheric physics at the Research Center for Climate and Atmosphere) rendered essential guidance throughout the research process, providing critical instructions and recommendations pertinent to research methodology, data interpretation, and augmenting the study. **Satria Bijaksana** (PhD, Professor of Rock Magnetism) rendered vital counsel and constructive feedback pertinent to both the research and drafting phases, offering insight on theoretical dimensions and fortifying the overall interpretation and methodological rigour of the investigation. **Rizal Suryana** (MSc, Researcher at Aeronautics and Space Research Center) facilitated data acquisition. **Khalil Ibrahim** (MEng, Geophysical engineer with expertise in geophysical exploration) participated in editing the draft. **Ulvienin Harlianti** (Dr, Geophysical engineer with expertise in rock magnetism and geochemistry for environmental purposes) participated in editing the draft.
All authors have read and agreed to the published version of the manuscript.